scientific reports

OPEN

Endosomal microautophagy is activated by specific cellular stresses in trout hepatocytes

Emilio J. Vélez[1,3,4✉], Vincent Véron[1,4], Jeanne Gouis[1], Steffi Reji[1], Karine Dias[1], Amaury Herpin[2], Florian Beaumatin[1] & Iban Seiliez[1✉]

Endosomal microautophagy (eMI) is a recently discovered autophagic process where cytosolic proteins are selectively captured in late endosome/multivesicular bodies (LE/MVB). This pathway, similar to chaperone-mediated autophagy (CMA), involves the recognition of KFERQ-like motif containing proteins by HSC70. While CMA targets substrates to lysosomes via the receptor LAMP2A, eMI involves internalization into intraluminal vesicles within LE/MVB through interactions with ESCRT machinery. Although the same proteins could be targeted by either pathway, eMI's role in cellular homeostasis is less understood. Our research identified an eMI-like process in rainbow trout hepatocytes, triggered by oxidative stress, high-glucose, DNA damage, and nutrient deprivation, but not serum deprivation. This finding suggests eMI's stimulus-specific induction and its potential compensatory role when CMA is impaired. Our study provides new insights into eMI and offers novel model organisms for exploring its interactions with CMA, enhancing our understanding of cellular stress responses.

Abbreviations

CMA	Chaperone-mediated autophagy
CQ	Chloroquine
eMI	Endosomal microautophagy
HG	High-glucose
LAMP2A	Lysosomal associated membrane protein 2A
LE	Late endosome
MA	Macroautophagy
Mo	Morpholino oligonucleotide
MVB	Multivesicular bodies
PCC	Pearson's correlation coefficient
RAB7	Ras-related protein 7
RT	*Oncorhynchus mykiss*

Endosomal microautophagy (eMI) is a recently discovered autophagy process in which cytosolic proteins are selectively trapped in vesicles formed at the membrane level of late endosomes (LE)[1]. eMi can be considered as the "sister" pathway of the more studied chaperone-mediated autophagy (CMA)[2], as both are characterized by the selective targeting of cytosolic proteins containing a pentapeptide sequence biochemically similar to KFERQ (lysine-phenylalanine-glutamate-arginine-glutamine)[3]. Both processes initiate with the recognition of a KFERQ-like motif by HSC70 (heat shock protein family A (Hsp70) member 8, also known as HSPA8) and co-chaperones[4–6]. For CMA, after binding to the limiting CMA receptor LAMP2A (lysosomal associated membrane protein 2A)[7,8], the substrates are targeted and translocated into lysosomes for degradation. In contrast, during eMI, the substrate is targeted to the LE membrane via the binding to negatively charged phosphatidylserine residues[2]. The cargo is then internalized thanks to the mediation of some members of the ESCRT machinery (Tsg101 and Alix) and the ATPase Vps4, forming multivesicular bodies (MVB)[1,9,10]. Afterwards, the KFERQ-containing protein can be degraded directly within LE/MVB, or after the fusion of these with lysosomes. Otherwise, the substrate can also be secreted after the fusion of LE/MVB with the plasma membrane[11–13].

[1]INRAE, Université de Pau et des Pays de l'Adour, UMR1419 Nutrition Métabolisme et Aquaculture, 64310 Saint-Pée-sur-Nivelle, France. [2]INRAE, UR1037 Laboratory of Fish Physiology and Genomics, 35700 Rennes, France. [3]Present address: Department of Cell Biology, Physiology and Immunology, Faculty of Biology, University of Barcelona, Barcelona, Spain. [4]Emilio J. Vélez and Vincent Véron contributed equally to this work. ✉email: evelezve@ub.edu; iban.seiliez@inrae.fr

Although the characteristic KFERQ-like motif, required for eMI and CMA targeting, is present in up to 75–80% of the total proteome from yeast to mammals[14], it is particularly noteworthy that this motif is present in key proteins involved in the control of transcription, cell cycle and cellular energetics, among others key cellular processes[6,14]. Thus, through the selective degradation of those motif-bearing proteins, eMI could play a critical role in maintaining cellular homeostasis and metabolism, as demonstrated for CMA[15–22]. In this regard, CMA malfunction has been associated with diverse pathological situations[23–27], and similarly, the reduction of eMI during aging has been associated with the progression of some proteinopathies[12,28,29]. Consequently, the interaction between both pathways in targeting KFERQ proteins could be a key step in the adequate remodeling of the cellular proteome during health and disease. For example, the KFERQ-containing protein TAU, linked to cellular senescence and brain disorders (tautopathies)[30], can be degraded through both CMA and eMI[29], and during CMA impairment, acetylated TAU is rerouted to eMI[12]. Therefore, exploring the specificities of the regulation of both pathways could reveal novel aspects about the control of metabolism and cellular homeostasis. For instance, eMI and CMA are reciprocally regulated during sustained starvation[9,31], pointing to a specialization of functions, action scenarios or preferred targets between these two autophagic pathways that deserve further research.

Recently, we provided functional evidence for the existence of a CMA pathway in fish, opening new perspectives for approaching this function from both novel and evolutionary perspectives[27]. This discovery highlighted the compelling need of using new models organisms, such as zebrafish (*Danio rerio*)—a powerful model for functional studies—and rainbow trout (RT, *Oncorhynchus mykiss*)—a model species with impaired glucose tolerance – to better decipher the fundamental processes engaged in this function[20–22]. In contrast, the ability of fish to perform eMI has so far not been reported nor explored[32]. However, our latest research in RT revealed that in vitro silencing of the CMA-limiting factor *lamp2a* led to significantly increased levels of the endosomal sorting complexes required for transport-I (ESCRT-I) protein tumor susceptibility 101 (Tsg101)[20], critical for eMI in mammals[1]. This suggested that an eMI-like process may compensate for impaired CMA activity, as seen in mammals[9,12]. Here, using a fluorescent eMI reporter originally developed for fruit flies[33], we identified and characterized an eMI-like pathway in a RT hepatocyte cell line. Under mild-oxidative stress, the fluorescent biosensor accumulated in puncta that co-localized with LE. Interestingly, while the formation of these KFERQ-like motif-dependent puncta is directly related to the ESCRT machinery, it has noteworthy been shown to be totally independent of CMA and macroautophagy (MA). We also found the RT eMI-like process was triggered by hyperglycemic stress, DNA damage and nutrient deprivation, but not by foetal bovine serum (FBS) removal, showing selective induction. In summary, these results demonstrate for the first time the presence of an eMI-like process in fish, offering new opportunities and models to study this autophagic pathway and its interactions with CMA.

Results and discussion
The core eMI machinery is expressed in fish tissues and RTH-149 cells
eMI process requires KFERQ-like motif recognition by HSC70 and interaction with other key components, including the ESCRT-I protein TSG101 and its associated protein ALG-2 Interacting Protein X (ALIX), the ATPase Vacuolar Protein Sorting 4 (VPS4), as well as the chaperone protein Bag Cochaperone 6 (Bag6)[9]. While HSC70 is highly conserved across phyla[32], the presence of other eMI components in fish genomes has not been evaluated. Interestingly, during evolution, teleost fish underwent a third round of genome duplication (Ts3R). Additionally, salmonids, including RT, experienced a four round of whole-genome duplication (Ss4R) (Fig. 1A)[34]. As a result, up to four orthologs of each human gene might be expected in the RT genome. Homology-based searches in the RT genome (Ensembl release 112) identified several genes with high homology to human *TSG101*, *VPS4A*, *VPS4B*, *ALIX* and *BAG6*. While only one ortholog of *TSG101* has been retained in the RT genome (Fig. 1B), we identified two orthologs for *VPS4A* and *ALIX*, and four copies for *VPS4B* and *BAG6* (Fig. 1B). Using the *PhyloFish* RNA-seq database, which provides gene expression data from different ray-finned fish species[35], we screened for expression of those genes across different RT tissues (Fig. 1C). We detected mRNA expression of all genes, particularly in the brain, gills, kidney and ovary, with levels varying by tissue and gene. We also analyzed the expression of those genes in the RT liver cell line RTH-149 (Fig. 1C red inset), finding that *tsg101*, *vps4a*C2, *vps4a*C1, *vps4b*C8, *vps4b*C28, *Alix*C18, and the four RT *bag6*s are expressed in this model. Thus, the RTH-149 cell line emerges as an interesting system to further dissect this process using in vitro tools. Taken together, these results reveal that the RT displays and express the core machinery involved in the formation of multivesicular bodies, an essential step in eMI, suggesting that this species would have the genetic potential to perform an eMI-like process. Moreover, using the same strategy, we have identified corresponding orthologs in zebrafish (Supplementary Fig. 1A) and confirmed their tissue-dependent expression (Supplementary Fig. 1B). These results suggest that the potential to perform an eMI-like process is not exclusive to RT but a common feature of teleost fishes.

Mild-oxidative stress induces eMI-like puncta that co-localize with LE in RTH-149 cells
Recently, we demonstrated that mild-oxidative stress induces recognition of a KFERQ-fluorescent reporter by chaperones for its targeting and degradation by CMA in RTH-149 cells[20]. Here, we have used an eMI-reporter previously employed to track eMI in flies and mammals[29,33]. It consists in a KFERQ recognition motif fused to either the N-terminal or C-terminal of the split Venus. While hemi KFERQ-tagged Venus proteins can be unfolded and rapidly degraded in lysosomes by CMA, resulting in no fluorescence, they would fluoresce only when the N- and C-terminal parts are reconstituted in close proximity within the MVB during eMI[29]. Here, we generated RTH-149 cells that stably express both KFERQ-split Venus proteins, and tested whether mild-oxidative stress (H_2O_2, 25 μM) could induce an eMI-like process, as observed in flies[36]. Under control (CT) conditions, the eMI sensor displayed a diffuse distribution with only few discrete and scattered puncta (Fig. 2A;
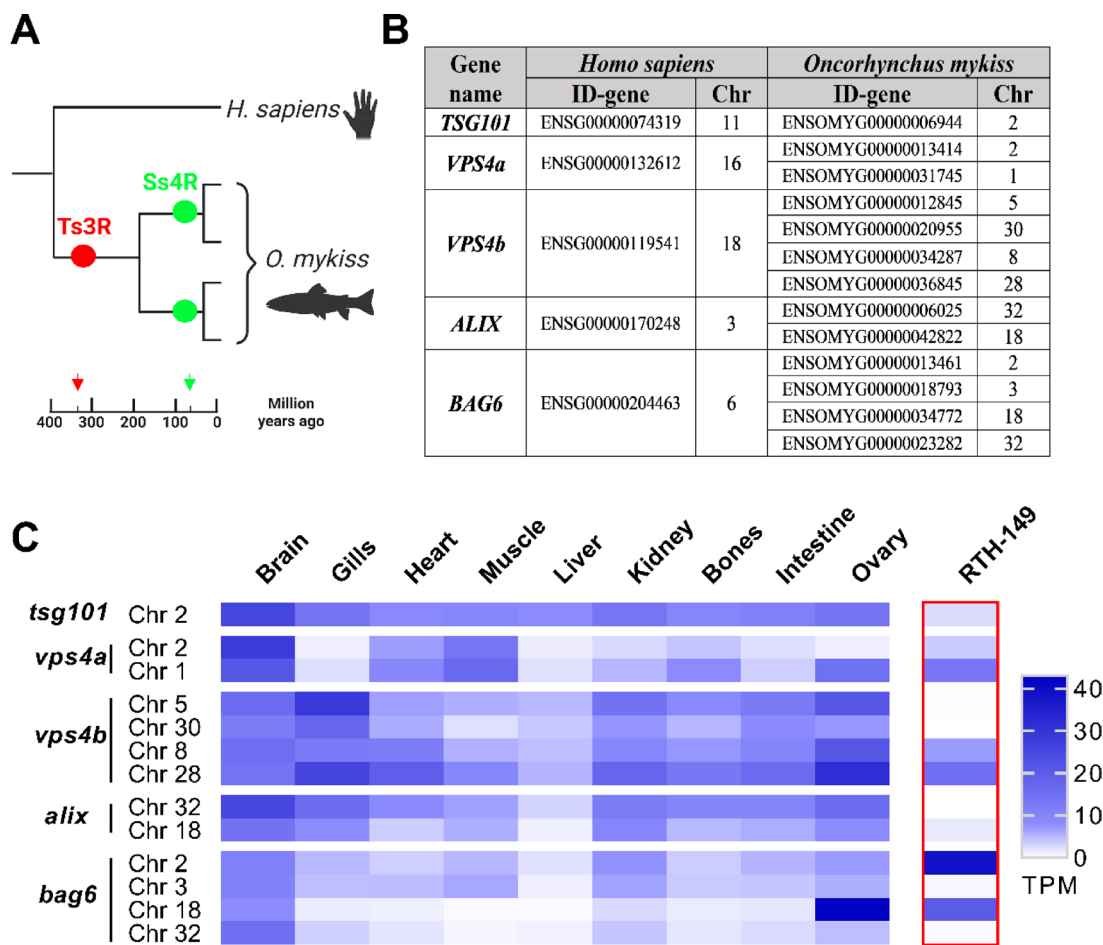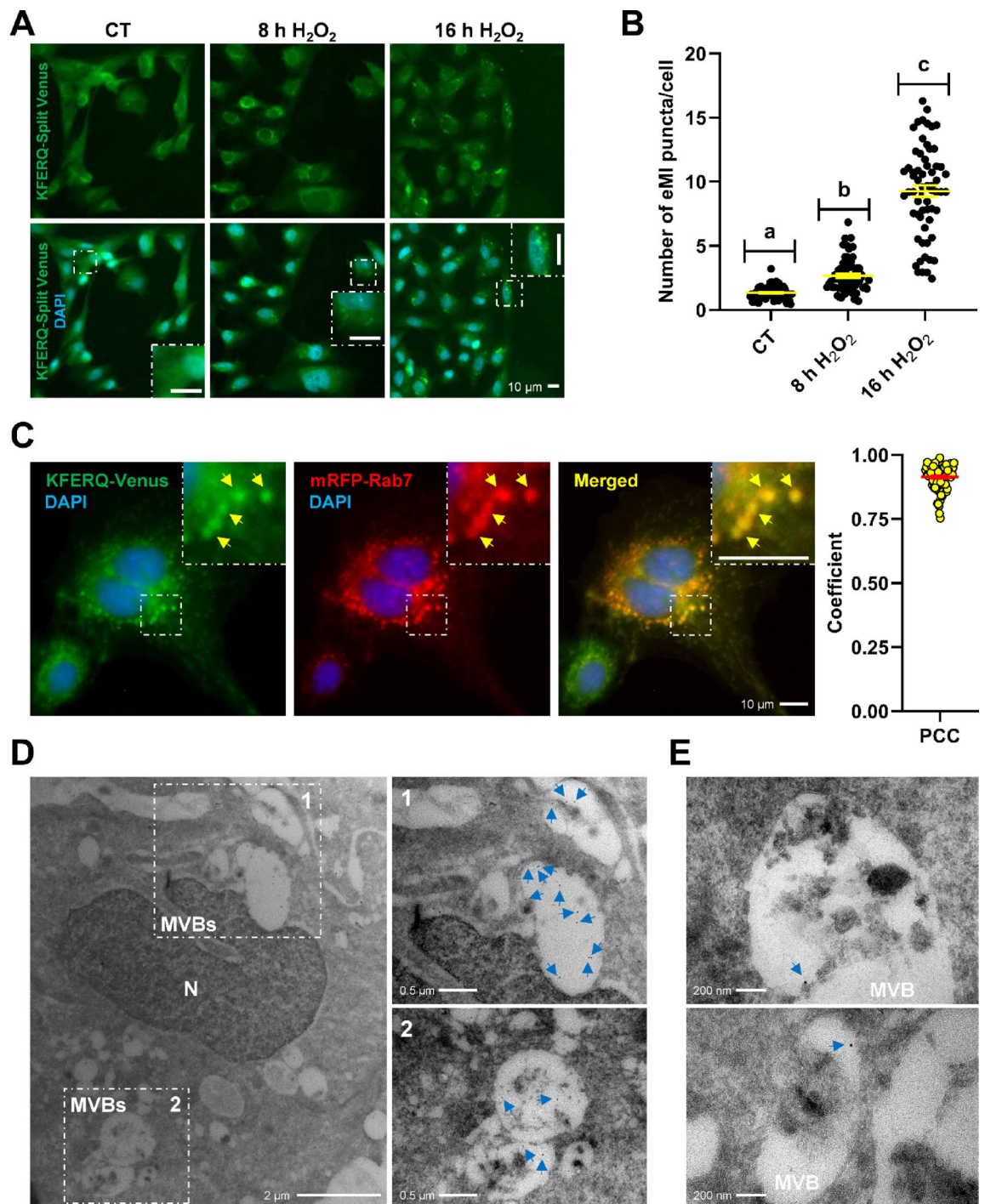
Fig. 1. The core eMI machinery is present and expressed in *Oncorhynchus mykiss* (RT, rainbow trout) tissues and the RT-derived RTH-149 cells. (**A**) Schematic representation of the evolutionary history of RT genes showing the third round of genome duplication (Ts3R) experienced by teleost fish, and the additional round of whole-genome duplication (Ss4R) of salmonids. (**B**) Identification (Ensembl ID) and chromosome location (Chr) of the main eMI-genes (*TSG101*, *VPS4A*, *VPS4B*, *ALIX* and *BAG6*) in the human genome, and their corresponding RT orthologs. (**C**) Heat map showing mRNA expression levels (TPM, transcripts per million) of the different identified genes in different tissues of RT (brain, gills, heart, muscle, liver, kidney, bones, intestine and ovary) extracted from the RNA-Seq database PhyloFish, as well as in RTH-149 cells (framed with red line) analyzed by BRB-Seq in the current work.

quantification in Fig. 2B). In contrast, H_2O_2 treatment for 8 or 16 h resulted in higher numbers of Venus puncta, showing a clear time-response effect (Fig. 2A; quantification in Fig. 2B). To widely locate these H_2O_2-induced Venus puncta, we assessed their co-occurrence with the LE marker RAB7 (Ras-related protein 7)[9,57] labelled with RFP. We found a high level of co-occurrence between eMI-sensor puncta induced by mild-oxidative stress and the RAB7 signal (Fig. 2C). The positive Pearson's correlation coefficient between the intensity of the two fluorescent channels (PCC, Mean ± SEM: 0.914 ± 0.004 from a total of 85 cells RAB7 +) supported their co-occurrence[38]. Finally, to gather more evidence on the subcellular localization of the eMI-sensor puncta following mild-oxidative stress in RTH-149 cells, we performed an immuno-electron microscopy (IEM) study using gold-tagged antibodies to assess the presence of Venus proteins (Fig. 2D and E). The images showed immunogold labeling of this fluorescent eMI reporter within MVBs, further supporting its internalization in MVBs.

These results suggest that mild-oxidative stress in RT cells induces the targeting of KFERQ-containing proteins to LE in a process similar to eMI in flies and mammals[6].

The occurrence of eMI-like puncta under mild-oxidative stress depends on KFERQ-like motif and relies on ESCRT machinery but not on CMA nor on MA

To determine if the Venus puncta co-occurring in response to oxidative stress corresponds to an indeed exclusive eMI-like activity, more evidence on the specificity of these observations is required. First, we investigated whether Venus puncta formation requires the presence of the KFERQ-like motif. To that end, we generated new eMI-reporter constructs in which the KFERQ motif was mutated to a non-functional KFEAA sequence[39], and using antibiotic selection we generated RTH-149 cells stably expressing both KFEAA-split N-Venus and KFEAA-split C-Venus proteins. While this new reporter could show bulk-eMI activity, KFEAA-Venus proteins

cannot be internalized to LE/MVBs by selective eMI. When we compared the formation of Venus puncta between cells expressing the KFERQ motif or instead the non-functional KFEAA sequence in presence of H_2O_2 treatment, we found that the numbers of puncta per cell were significantly hampered when the KFERQ motif was mutated (Fig. 3A; quantification in Fig. 3B). This result demonstrated the KFERQ-motif selectivity of this RT eMI-like process. Then, we explored the dependence of this process on the ESCRT machinery. Hence, siRNA were designed to target RT *tsg101* mRNA, which encodes an essential protein of the ESCRT-I complex[1]. This siRNA (si*tsg101*) efficiently knocked down *tsg101* gene expression in RTH-149 cells (Supplementary Fig. 2A) and reduced its protein levels (Fig. 3C; quantification in Fig. 3D). Transfection of RTH-149 cells expressing both hemi-KFERQ-Split Venus constructs with negative control siRNA (si*LUC*) did not affect H_2O_2-induced puncta formation (Fig. 3E; quantification in Fig. 3F). However, si*tsg101* prevented the formation of the Venus-puncta. Moreover, siRNAs targeting the two essential and limiting CMA receptors (*lamp2a*-C14 and *lamp2a*-C31), previously validated[20] and confirmed here (Supplementary Fig. 2B, quantification in Supplementary Fig. 2C), did not alter Venus puncta formation (Fig. 3E; quantification in Fig. 3F). Interestingly, blocking CMA with si*lamp2a* significantly ($p < 0.001$) increased the number of H_2O_2-induced Venus-puncta compared to si*LUC* (Fig. 3F), suggesting CMA absence might be compensated by an eMI-like process. This aligns with our prior study, which

◀**Fig. 2**. Mild-oxidative stress (H_2O_2 25 μM) induced the targeting of the eMI-reporter Venus to late endosomes through an eMI-like process in RT cells. (**A**) Representative images of RTH-149 cells stably expressing an eMI-reporter consisting in a KFERQ recognition motif fused to either the N-terminal or C-terminal of split Venus and visualized by fluorescence microscopy. The exposure to H_2O_2 25 μM, for either 8 h or 16 h, induced the reconstitution of the Venus fluorescent protein (green) and the formation of Venus-puncta, in comparison with the CT, where the reporter showed a diffuse distribution with only discrete and scattered puncta standing out from the background noise. Nuclei were stained with DAPI (blue) and the inset show an amplified region of each image. (**B**) Quantification of KFERQ-Venus number of puncta per cell. All values correspond to individual images (CT 63; 8 h H_2O_2 63; 16 h H_2O_2 63), with > 18 images/experiment in a total of 3 independent experiments (> 600 cells per condition). Different letters denote significant differences between groups compared by the non-parametric Kruskal–Wallis test (p < 0.0001) followed by Dunn's multiple comparisons tests. All data are presented as Mean ± SEM; scale bars: 10 μm. (**C**) Representative images of H_2O_2-induced KFERQ-Venus puncta (green) in cells transiently transfected with RAB7-RFP (red) visualized by fluorescence microscopy. Most of the KFERQ-Venus puncta co-localized with the red late endosome marker RAB7-RFP, as indicated by the yellow arrowheads and amplified in the insets, and as supported by the positive Pearson's correlation coefficient (PCC) results of the global analysis of 85 single cells using the BIOP version of JACoP plugin for Fiji. Scale bars: 10 μm. (**D**) Representative immunoelectron microscopy images of H_2O_2-incubated RTH-149 cells expressing the eMI sensor (Venus) using anti-Venus antibody, showing Venus immunoreactivity (arrowheads in the amplified insets) within MVBs. Scale bars: 2 μm or 0.5 μm (insets). (**E**) Other two representative IEM images at a higher magnification showing Venus immunoreactivity (arrowheads) within MVBs. Scale bar: 200 nm.
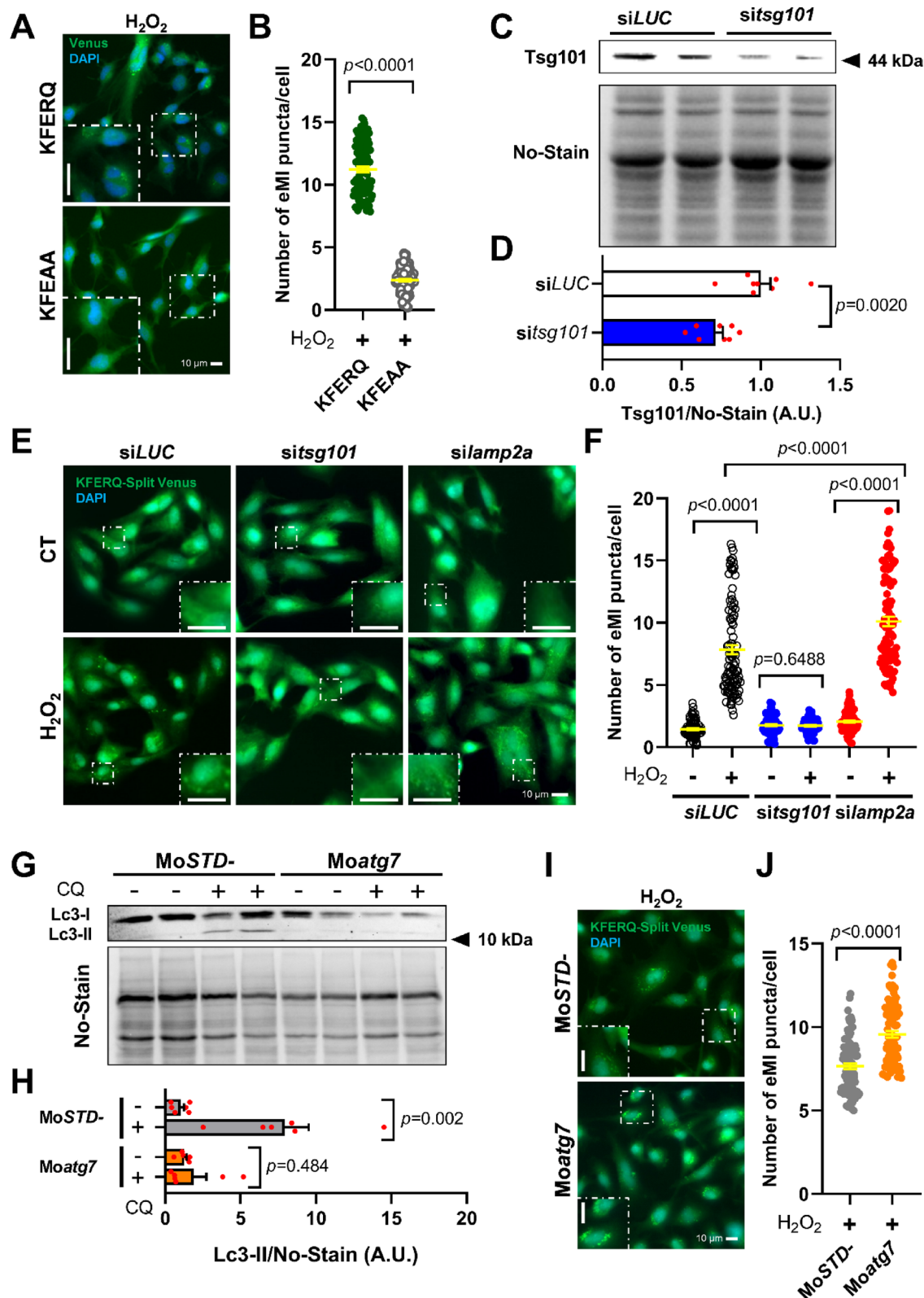
showed increased Tsg101 levels following in vitro silencing of *lamp2a*[20]. Similarly, *tsg101* knockdown increased H_2O_2-induced CMA-puncta compared to si*LUC* (Supplementary Fig. 2C), suggesting reciprocal compensation between these pathways for degrading KFERQ-containing proteins when one is impaired. This crosstalk between autophagy pathways was also reported in mammals, where Bag6 plays a key role in switching between them[9]. In this sense, that study evidenced that the CMA-mediated degradation of the chaperone BAG6 inhibits eMI in rodents. Aiming to explore whether this chaperone, whose interaction in mammals with members of the ESCRT-I complex (i.e., Tsg101) appears essential in the eMI process[9], is key for the formation of these eMI-like puncta in the RT, we designed a cocktail of morpholino oligonucleotides (Mo) intended to disrupt the splicing process of all pre-mRNA of the four RT paralogs of *BAG6* (Fig. 1B) at the same time (Mo*bag6*). We found that this strategy led to a marked reduction in the overall *bag6* mRNA levels in RTH-149 cells (Supplementary Fig. 2D). Then, we observed that transfection of RTH-149 cells expressing the eMI sensor with Mo*bag6* significantly prevented the formation of Venus-puncta after mild-oxidative stress exposure (Supplementary Fig. 2E; quantification in S2F) when compared with standard negative control Mo (Mo*STD*-) transfected cells. This result supports that Bag6 protein is essential for the formation of Venus puncta in RT cells, as recently reported in rodents[9], and provide further evidence on the RT eMI-like process dependence on the ESCRT-I complex machinery. Future studies should address whether Bag6 is solely a key regulator of eMI activity in RT, or whether it also plays a role as switcher, directing KFERQ-containing proteins to either eMI or CMA and enabling these pathways to compensate for each other's deficiencies as observed in mammals[9].

To next evaluate whether the KFERQ- and ESCRT-I-dependent but CMA-independent eMI-like puncta might also rely on MA, we designed a Mo to inhibit the translation of mRNAs encoding the E1-like enzyme Atg7 in the RT. This approach aims to impair MA initiation[40]. First, we found that the reduction of Atg7 by Mo*atg7* led to a significant reduction in the conjugation of Atg5 to Atg12 (Supplementary Fig. 2G and H), a key process in MA initiation recognized to be dependent on the activity of Atg7[41]. Besides, we assessed LC3 lipidation as a readout of the MA flux after exposing cells to H_2O_2, with or without the autophagosome-lysosome fusion inhibitor chloroquine (CQ, at 10 μM)[42]. Mo*atg7* markedly reduced LC3-II levels compared to cells transfected with the negative control oligo (Mo*STD*–) (Fig. 3G; quantification in Fig. 3H). Together with the loss of Atg12–Atg5 complex formation, this confirmed effective MA inhibition. We then examined Venus-puncta formation under mild-oxidative stress and observed that MA inhibition did not decrease the number of eMI-sensor puncta (Fig. 3I, quantification in Fig. 3J). Instead, it increased the puncta count compared to Mo*STD*-, similar to findings in *Drosophila* fat body[36]. This suggests that increased cellular stress might enhance eMI-like process in RT as well.

Together, our results demonstrate that the formation of the KFERQ-Venus puncta upon H_2O_2 incubation specifically relies on ESCRT-I machinery but is indeed independent of both CMA and MA activities, supporting -for the first time- the existence of an eMI-like process in fish. Interestingly, we have observed that the activity of such process in RT increases when either CMA or MA are impaired, which points to an established and probably finely tuned crosstalk between these autophagy pathways to maintain cellular proteome homeostasis. This interaction certainly warrants further research.

eMI induction in RT is stimulus-specific

As reviewed by Wang et al.[2], eMI induction appears to be stimulus-specific. In *Drosophila*, eMI is triggered by prolonged nutrient starvation[43], oxidative stress, or DNA damage[36]. In mammals, eMI can be stimulated by iron starvation and DNA damage[11,37], but unlike in *Drosophila*, it is either unaffected or downregulated during nutrient deprivation[1,9]. In this study, we examined the effect of different cellular stresses on eMI-sensor puncta formation in RTH-149 cells. We found that high-glucose (HG) treatment, similar to H_2O_2, increased the number of Venus puncta compared to the CT condition (Fig. 4A, quantification in Fig. 4B). We recently showed that

HG induces oxidative stress in these cells, mirroring H_2O_2 effects, and reflecting the glucose intolerance typical of RT[20]. Notably, existing data from *Drosophila* suggest a MAPK/JNK signaling involvement in eMI induction during oxidative stress[36]. However, the potential role of NRF2 cannot be ruled out, as demonstrated for CMA in mammalian cells[44], and more recently in RTH-149[20]. Future research should explore if this mechanism is conserved in RT.

We then examined the effect of genotoxic insults by inducing DNA double-strand breaks with etoposide (50 µM)[45]. Our results showed that etoposide clearly increased Venus puncta compared to CT (Fig. 4A, quantification in Fig. 4B), similarly to findings in *Drosophila*[36] and mammals[37]. In mammals, CMA participates

◄**Fig. 3**. The occurrence of eMI-like puncta under mild-oxidative stress depends on the KFERQ motif and the ESCRT machinery, but not on CMA nor on MA. (**A**) Representative images of RTH-149 cells expressing either the KFERQ-Venus proteins or their mutated versions (i.e., KFEAA-Venus) and exposed to H_2O_2 25 μM for 16 h, and (**B**) quantification of the corresponding number of Venus puncta per cell. All values correspond to individual images (KFERQ 94; KFEAA 96), with > 30 images/experiment in a total of 3 independent experiments (> 2000 cells per condition). Differences between the two groups were assessed using Mann Whitney test ($p < 0.0001$). Transfection of RTH-149 cells with si*tsg101* reduced significantly the proteins levels of Tsg101, as it can be observed in (**C**) the representative western blot image of Tsg101 and the total protein stain (No-Stain), and (**D**) the densitometry quantification of Tsg101 normalized with No-Stain. Differences with respect to the si*LUC* were assessed using Unpaired Student's T-test ($p < 0.002$) in four independent experiments with duplicates. (**E**) Representative images of RTH-149 cells expressing the eMI-reporter transfected with either negative control siRNA (si*LUC*), si*tsg101*, or a combination of two siRNAs targeting the two *lamp2a* paralogs (si*lamp2a*) of RT, and incubated with CT medium or exposed to mild-oxidative stress (H_2O_2 25 μM) for 16 h, and the (**F**) quantification of KFERQ-Venus number of puncta per cell. All values correspond to individual images (si*LUC* CT 96; si*LUC* H_2O_2 101; si*tsg101* CT 96; si*tsg101* H_2O_2 96; si*lamp2a* CT 96; si*lamp2a* H_2O_2 95), with > 31 images/experiment in a total of 3 independent experiments (> 600 cells per condition). Differences between two groups were assessed using parametric Unpaired Student's T-test or the non-parametric Mann Whitney test, and the *p* values are indicated in the figure. (**G**) Representative image of western blot against LC3B in RTH-149 cells transfected with a morpholino oligonucleotide (Mo) targeting RT Atg7 (Mo*atg7*) or a negative control (Mo*STD-*), exposed during 16 h to H_2O_2 25 μM and additionally incubated with or without 10 μM chloroquine (CQ), and (**H**) quantification of LC3-II protein levels normalized to No-Stain. Differences between groups were assessed using parametric Unpaired Student's T-test (Mo*atg7* group) or non-parametric Mann Whitney test (Mo*STD-*) in three independent experiments with duplicates. (**I**) Representative images of RTH-149 cells expressing the eMI-reporter transfected with either Mo*STD-* or Mo*atg7* and exposed to H_2O_2 25 μM for 16 h, and (**J**) quantification of KFERQ-Venus number of puncta per cell. All values correspond to individual images (Mo*STD-* 88; Mo*atg7* 90), with > 21 images/experiment in a total of 3 independent experiments (> 600 cells per condition). Differences between the two groups were assessed using Mann Whitney test ($p < 0.0001$). All data are presented as Mean ± SEM; scale bars: 10 μm.
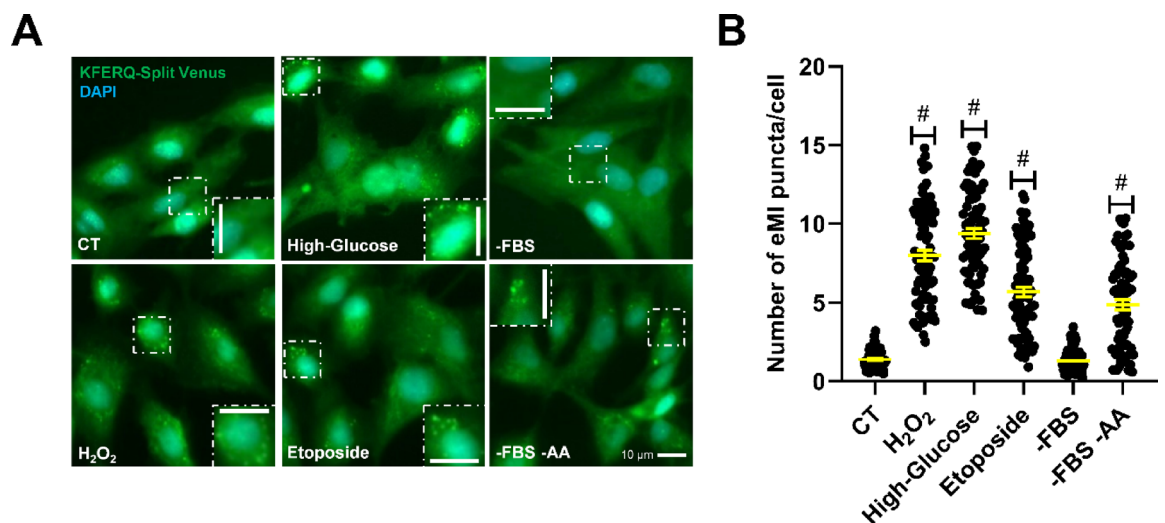

Fig. 4. Different cellular stressors, although not serum starvation, activated eMI-sensor puncta formation in RTH-149 cells. (**A**) Representative images of RTH-149 cells expressing the eMI-reporter and incubated for 16 h with either CT medium, H_2O_2 (25 μM), glucose (25 mM, High-Glucose), etoposide (50 μM), a medium lacking serum (-FBS) alone, or a medium lacking both serum and amino acids (-FBS –AA). (**B**) Quantification of KFERQ-Venus number of puncta per cell. All values correspond to individual images (CT 80; H_2O_2 86; High-Glucose 76; Etoposide 86; –FBS 87; –FBS –AA 76), with > 15 images/experiment in a total of 3 independent experiments (> 600 cells per condition). Differences between two groups were assessed using the non-parametric Mann Whitney test, and the *p* values are indicated in the figure. All data are presented as Mean ± SEM; scale bars: 10 μm.

in the selective degradation of the checkpoint kinase 1 (Chk1), a KFERQ-motif containing protein, to ensure cell cycle progression after DNA repair[46]. Conversely, CMA impairment was associated with defects in nuclear proteostasis, genomic instability and reduced cell survival[46]. Although it remains to be determined whether Chk11 can also be targeted by eMI, these findings suggest a conserved protective mechanism that maintains

genome integrity through the degradation of KFERQ-substrates after DNA damage, which could be, at least partly, fulfilled by eMI in RT.

Finally, we observed that serum starvation (-FBS), known to induce both CMA[3,39,47] and MA in various species, including RT[48–50], did not alter Venus-puncta formation. In contrast, combined serum and amino acids deprivation (-FBS -AA) with HBSS medium for 16 h substantially increased eMI-like puncta compared to CT (Fig. 4A, quantification in Fig. 4B). This aligns with increased eMI during prolonged nutrient deprivation in the CMA-deficient species *Drosophila*[43]. In mammals, where both CMA and eMI pathways are present, the regulation of eMI during nutrient deprivation is more complex[28]. Short-time (1 h) HBSS exposure triggers an ESCRT-III-dependent, but ESCRT-I and Hsc70-independent, eMI variant in human cell lines. This variant likely degrades selective autophagy receptors (e.g., LC3B and GABARAPL2), preventing unwarranted selective MA in the short-term, while enhancing bulk MA during prolonged starvation[51]. Conversely, long-term nutrient starvation, a well-known CMA activator[31], inhibits eMI in rodents, likely due to the CMA-mediated degradation of the eMI component BAG6[9]. This research highlights the possible role of BAG6 as a switcher, directing KFERQ-containing proteins to either eMI or CMA and enabling these pathways to compensate for each other's deficiencies. In RT, although the silencing of *bag6* appears to inhibit the eMI process similar to what was observed in mice[9], both autophagic pathways function simultaneously during stress, such as mild-oxidative stress and nutrient deprivation (16 h), targeting KFERQ-containing proteins to lysosomes and LE/MVB. This raises the question of whether a Bag6-dependent mechanism coordinates both eMI and CMA pathways in RT as observed in mammals. However, the differences between our results and those in mammals may stem from the experimental models used. In our in vitro model, -FBS -AA represents an acute condition with negligible extracellular levels of these compounds, while mammalian studies involved in vivo nutrient starvation experiments[9], where circulating nutrient and growth factor levels likely remain physiological. To the best of our knowledge, no data exists on the in vitro activity of eMI in mammals during both long-term and acute nutrient deprivation. Therefore, we cannot ruled out that the simultaneous activation of CMA and eMI observed in the present study may be a conserved physiological response regarding extreme cellular stress across vertebrates.

In summary, we identified and characterized an eMI-like pathway in a RT hepatocyte cell line. This process is induced by oxidative stress, DNA damage, or nutrient deprivation, mirroring findings in *Drosophila*[36,43], but not in response to FBS removal, supporting that eMI induction in RT is stimulus-specific. These findings suggest a significant role for this eMI-like process in fine-tuning the cellular proteome during stress in RT. Moreover, they open new avenues for exploring this function using complementary model organisms, such as zebrafish and RT.

Materials and methods
Laboratory ware and reagents
Minimum Essential Medium (61,100-053), essential (11,130-036) and non-essential amino acids (11,140–050), L-glutamine (25,030-024), sodium pyruvate (11,360-070), penicillin–streptomycin (15,140-122), geneticin (11,811,031), neomycin (11,598,906), puromycin (10,296,974), fetal bovine serum (10,270-106), and Hank's Balanced Salt Solution (14,025-092), were all purchased from Gibco. HEPES (BP299-1) and PBS (BP2944) were procured by Fisher BioReagents. Hydrogen peroxide solution (H1009), D-(+)-Glucose (G7021) and chloroquine (C6628) were all purchased from Sigma-Aldrich. Etoposide (HY-13629) was purchased from MedChemExpress, paraformaldehyde 4% fixative (22,023) from Biotium, and the antifade mounting medium containing DAPI (H-2000) from Vector Laboratories, Inc. The TRIzol Reagent (15,596,018), RIPA buffer (89,901), the cocktail of protease and phosphatases inhibitors (78,422), the Qubit protein assay kit (Q33211), SuperBlock Blocking Buffer in PBS (37,515), SuperSignal West Pico Plus Chemiluminescent Substrate (34,578), and No-Stain Protein Labeling Reagent (A44449), were all acquired from ThermoFisher Scientific. All laboratory plastic ware, unless otherwise stated, were procured by Sarstedt AG & Co. KG.

Bioinformatics analysis, oligos and plasmids
Ensembl Genome database (Ensembl release 112; http://www.ensembl.org) was used to identify orthologous genes to the human genes coding for the main eMI players in the genome of RT (Genome assembly: USDA_OmykA_1.1), or of *Danio rerio* (Genome assembly: GRCz11), and their identity was later confirmed using Genomicus version 110.01[52]. To screen whether the identified genes are expressed across different tissues of RT and zebrafish, we interrogated the PhyloFish RNA-seq database[35]. Instead, to evaluate their expression in RTH-149 cells, we performed a Bulk RNA barcoding and sequencing (BRB-seq) analysis[53] using the services of Alithea Genomics S.A as explained below.

Regarding oligos, up to four new siRNAs against the RT *tsg101* mRNA sequence (Ensembl ID-gene: ENSOMYG00000006944) were designed using the siDESIGN Center. After testing their efficiency in reducing both mRNA and protein levels of Tsg101 by qPCR and western blot (data not shown), the most effective was selected for following experiments (si*tsg101*; 5′-UGAUUAGGUGAGCGAAUUA-3′). The different siRNAs using in the present work, including the siRNAs against the two RT *lamp2a*'s (i.e., si*14*; 5′-UAAAGAAAUUGCUCGGCUC-3′, and si*31*; 5′- UGGAGAAGCGGCUGUGUUA-3′, previously validated for RT[20], and a negative control siRNA against LucGL2 (si*LUC*; 5′-CGUACGCGGAAUACUUCGA-3′), not expressed in RT cells, were purchased from Horizon Discovery. On the other hand, a morpholino oligonucleotide (Mo*atg7*; 5′-CAGAAGCCATCTCTATCACCG-3′) was designed in collaboration with GeneTools customer support to targeting the start codon of the RT *atg7* mRNA sequence (Ensembl ID-gene: ENSOMYG00000075941) for blocking its translation. Besides, two different splice junction-targeting morpholinos were designed, each directed against pairs of RT bag6 paralogs. The first targeted the paralogs located on chromosomes 2 and 3 (Ensembl gene IDs: ENSOMYG00000013461 and ENSOMYG00000018793; designated Mo*bag6*$_{chr2}$&$_{chr3}$; sequence: 5′-CAGACAGCATTACTCACTGTAC-3′). The second targeted the paralogs located on chromosomes 18 and 32 (Ensembl gene IDs: ENSOMYG00000034772 and ENSOMYG00000023282; designated Mo*bag6*$_{chr18}$&$_{chr32}$; sequence: 5′- TAGT

TGCTGGCTTTTTTACTCAC-3). A standard negative control morpholino (MoSTD-; sequence: 5′-CCTCTT ACCTCAGTTACAATTTATA-3′), targeting against an intronic region of the human β-globin gene associated with β-thalassemia, was also designed. All morpholinos were purchased from GeneTools.

Concerning plasmids, two constructions originally designed for tracking eMI in *Drosophila*[33] and based on the backbone pUAST-attB (RRID:DGRC_1419) plus the 21st amino acids of RNASe A, including its KFERQ motif, fused to either the N- or C-Split Venus[54], were gifted by Patrik Verstreken (KU Leuven). Those two plasmids were digested to isolate the N- and C-Split Venus regions tagged to the KFERQ motif, for their posterior sub-cloning in the backbone of the pEGFP-N1-ro1GFP [a gift from S. James Remington (Addgene plasmid #82369; http://n 2t.net/addgene:82369; RRID:Addgene_82369)] for a suitable expression in RT cells, but only after the removal of the EGFP sequence. The KFEAA-N-Venus was synthetized by Genewiz (Azenta Life Sciences) and inserted in the same pEGFP-N1-ro1GFP backbone detailed before. The KFEAA-C-Venus was also synthetized by Genewiz but inserted in the pCMV6-G2-ATP8-V5 plasmid [a gift from Matthew O'Connor (Addgene plasmid # 86852; http://n2t.net/addgene:86852 ; RRID:Addgene_86852). Moreover, mRFP-Rab7 plasmid was a gift from Ari Helenius (Addgene plasmid #14436; http://n2t.net/addgene:14436; RRID:Addgene_14436).

Cells and general experimental procedures

The RT hepatoma-149 cell line (RTH-149 cells; supplied by ATCC #CRL-1710; RRID:CVCL_3467), passage number below 20, and routinely screened to confirm absence of mycoplasma contamination by using the Myco-Sniff Mycoplasma PCR Detection Kit (MP Biomedicals #093050201) following the manufacturer's recommendations, was used for all cell culture experiments in the current work. This cell line has been previously validated as a reliable model for nutrition and autophagy research in the RT[20,49]. Cells were grown at 18 °C without CO_2 in complete medium (hereafter referred as control condition, CT) consisting in Minimum Essential Medium containing essential amino acids, 1X L-glutamine and glucose (5 mM), and supplemented with 1X non-essential amino acids, sodium pyruvate (1 mM), HEPES (25 mM), 1X Penicillin–Streptomycin, and 10% fetal bovine serum.

RTH-149 cells stably transfected with the two N- and C-Split Venus regions tagged to the KFERQ motif were selected for the resistance to the selective antibiotic geneticin, followed by cell sorting using a FACS Aria 2-Blue 6-Violet 3-Red 5-YelGr, 2 UV laser configuration (BD Biosciences, Le Pont de Claix Cedex, France) in biosafety cabinet. RTH-149 cells transfected to stably express the mutated KFERQ motifs (i.e., KFEAA-N-Venus and KFEAA-C-Venus) were selected for their resistance to both the selective antibiotics neomycin and puromycin. On the other hand, RTH-149 cells stably expressing a KFERQ-PA-mCherry1 generated and selected in our previous work[20] were additionally used for tracking CMA. Those eMI- or CMA-reporter cells, respectively, were maintained in a version of the CT medium detailed above in which the antibiotic used was geneticin. All the cells transfections with either plasmids (1–2.5 µg), siRNAs (1 µM) or morpholino oligos (5 µM), were performed with the Transfection System device (Invitrogen MPK5000) and Neon 100 µL samples Kit (Invitrogen MPK10096).

At the beginning of each experiment, similar to what was previously detailed in Vélez et al.[20], cells were counted using a Cellometer K2 device (Bioscience LLC, Lawrence, MA, USA) and plated at a density of 60.000 cells/well onto 4-well culture slides (Ibidi 80426 or FALCON 354114) for Venus or mCherry microscope imaging experiments, respectively. In the case ofRNA extraction and both protein collection and IEM experiments, cells were plated in 6-cm dishes at 400.000 or 500.000 cells/dish, respectively. Before experimental treatments, the cells were gently washed twice with 1X PBS, and then incubated with CT medium alone, or supplemented with either hydrogen peroxide (25 µM, H_2O_2 medium, mild-oxidative stress), High-Glucose (D-glucose at 25 mM), or etoposide (50 µM), as appropriate and for the times detailed elsewhere. Otherwise, cells were incubated with H_2O_2 medium supplemented with chloroquine (CQ condition, 10 µM), or instead, with 1X Hank's Balanced Salt Solution supplemented exclusively with HEPES (25 mM, HBSS condition, serum and nutrient starvation medium), or also with 1X essential amino acids, 1X non-essential amino acids, and 1X L-glutamine (-FBS condition, serum starvation medium). To asses CMA activity, the CMA-reporter expressing cells were photoactivated with a 405-nm light source for 10 min prior to starting the incubations[20].

Imaging procedures

Cells were fixed for 20 min using paraformaldehyde 4% before mounting and counterstaining nuclei with DAPI, and then the images were acquired in the Bordeaux Imaging Center (CNRS-INSERM and Bordeaux University, member of the national infrastructure France BioImaging). On the one hand, all cells images of KFERQ-Venus and mRFP-Rab7 fluorescence were acquired in widefield using a 20X/0.95 dry objective and a 1X intermediate lens with the high-content screening microscope Zeiss Cell Discoverer 7 (Zeiss Microscopy, Germany), which is equipped with Dual Zeiss Colibri LED-based illumination (from 385 to 625 nm), the dichroic mirrors 405/493/575/653, 450/538/610, 405/493/610, the emission filters 412-438/501-527/583-601/662-756, 458-474/546-564/618-756, 412-433/501-547/617-758, the color camera Zeiss Axiocam 512 as a detector, and its controlled by the Zen Blue 3.1 software (Zeiss). On the other hand, as reported before[20], for imaging CMA-reporter cells we used a widefield Microscope Leica DM 5000 (Leica Microsystems, Germany) equipped with a 40X/1.25 oil objective, DAPI and TRITC filter cubes, a Greyscale sCMOS camera (Hamamatsu Flash 4.0 V2, Japan), and controlled by MetaMorph v7.8.10.0 software (RRID:SCR_002368).

eMI-reporter puncta per image were automatically detected in the Venus-channel and counted with Fiji (RRID:SCR_002285) by using the ComDet v.0.5.5 plugin (developed in Cell Biology group of Utrecht University and available at https://github.com/UU-cellbiology/ComDet), with an approximate particle size of 4 pixels and an intensity threshold ranging from 5 to 20 SD as settings. Next, the number of nucleus (>100 pixels) in each image were counted by using the Fiji Analyze Particles function in the DAPI channel after IsoData thresholding and watershed segmentation. In the case of PA-mCherry1 fluorescence experiments, the CMA puncta were counted on images in gray (red channel) and blue (DAPI) by using the Cell Counter plugin of Fiji

(RRID:SCR_002285) as previously detailed[20], followed by nuclei counting. All images were counted in blind and random order and excluding cells on the edges or very superposed. For each image, the number of either eMI- or CMA-puncta was normalized by the number of nuclei within the image, and the results showed represent the number of puncta per cell in a minimum of 60 images coming from 3 independent experiments. In all cases, more than 600 cells/condition were counted.

The BIOP version (https://github.com/BIOP/ijp-jacop-b) of the original JACoP plugin (RRID:SCR_025164) for Fiji was used to evaluate the co-ocurrence between Venus-puncta and late endosomes labeled with mRFP-Rab7 in cells incubated with H_2O_2 medium. We analyzed in 85 single cells the PCC, which ranges from -1 to 1, where -1 indicates a negative correlation and $+1$ highlights a complete positive correlation, between the pixel-intensity of the two contrasted channels[38].

For IEM, cells were fixed for 1 h using a solution of paraformaldehyde 2% and glutaraldehyde 0.1% in PBS. After chemical fixation, cells were scrapped and pelleted in 12% gelatin. Small pieces were cut and incubated in 2.3M sucrose overnight at room temperature. Each sample were immersed in liquid nitrogen, and then sliced in ultrathin Sect. (70 nm) at -120 °C with a 35° angle diamond knife (Diatome®) and collected on nickel grid (Electron Microscopy Sciences). Immunogold labeling of Venus proteins were achieved on section with a goat anti-Venus polyclonal first antibody (Antibodies.com, A121679), followed by secondary antibody donkey-anti-goat IgG (H&L) coupled with a 10 nm gold particules (Aurion). At the end, contrasts were performed with a solution of 1% aqueous uranyl acetate in 2% methylcellulose for 10 min in ice in the dark. Sections were imaged using a Hitachi H7650 transmission electron microscope equipped with a Gatan Orius CCD camera, as previously described[55]. MVBs were identified using previously established criteria[56,57].

mRNA levels analysis: BRB-seq and quantitative RT-PCR

RNA samples were collected and processed with TRIzol reagent following the manufacturer's protocol. Then, RNA concentration was determined using a NanoDrop 2000 (Thermo Scientific) and integrity confirmed in an agarose gel, as previously reported[58]. In the case of Bulk RNA barcoding and sequencing (BRB-seq) analysis[53], 8 independent RNA samples (50 ng of RNA/each) were collected and isolated from RTH-149 cells cultured in growth medium and successively sent to Alithea Genomics S.A for its processing as explained in detail elsewhere[22]. On the other hand, for quantitative RT-PCR the samples were prepared as described before[49,55] and cDNA synthesis was performed in duplicate, followed by duplicated PCR analysis[20]. The relative quantification of the target gene *tsg101* and of all *bag6* paralogs was calculated using the ΔCT method[59] with *eef1a1* (eukaryotic translation elongation factor 1 alpha 1) as a reference gene. Primers used for *tsg101* (forward: 5′-CCAGTCAG CTACAGAGGAAACA-3′/reverse: 5′-AGATCTTGCCGTTGGCATCA-3′) and for all *bag6* paralogs (forward: 5′-CTGCAGGATGAGAGGAC-3′/reverse: 5′-TGCTGGTGCTGACTCTG-3′) were designed in the current work by using the Primer-Blast tool of NCBI, and the amplicons were sent to Genewiz (Azenta Life Sciences) to confirm primer specificity by Sanger Sequencing. Primers used for *eef1a1* (forward: 5′-TCCTCTTGGTCGTTT CGCTG-3′/reverse: 5′-ACCCGAGGGACATCCTGTG-3′) were previously validated[60].

Western blotting

Proteins were collected with RIPA buffer supplemented with protease and phosphatases inhibitor[49], and then quantified using a Qubit 2.0 fluorometer (ThermoFisher Scientific). Later, 5 μg of protein were separated by sodium dodecyl sulfate polyacrylamide gel electrophoresis (SDS-PAGE) and then proteins were transferred to polyvinylidene fluoride (PVDF) membranes (Merk-Millipore IPFL00010). Next, total protein labeling was performed with No-Stain Protein Labeling Reagent following the manufacturer's protocol for posterior accurate total protein normalization. After blocking membranes with SuperBlock Blocking Buffer in PBS, they were incubated with the corresponding primary antibody rabbit anti-TSG101 (Sigma-Aldrich HPA006161, at 1/500), rabbit anti-LC3B (Cell Signaling Technologies 2775, at 1/1000), or rabbit anti-ATG5 (Novus, NB110-53818), followed by incubation with a goat anti-rabbit secondary antibody HRP (Invitrogen 31460, at 1/10,000). Immunoreactive bands were developed thanks to the SuperSignal West Pico Plus Chemiluminescent Substrate, and imaged using Smart Exposure to assure signal linearity in an iBright FL1500 Imaging System (ThermoFisher Scientific). Finally, the images were quantified using the iBright Analysis Software (ThermoFisher Scientific, RRID:SCR_017632). Full-length blots are available in the supplementary Fig. 3.

Statistics and reproducibility

All statistical analyses in the current study were performed using GraphPad Prism (RRID:SCR_002798) version 8.0.1 for Windows (GraphPad Software, Inc., www.graphpad.com) considering a *p* value < 0.05 as a level of significance, and all data presented are reported as means ± SEM or fold induction respect the control group ± SEM, from a minimum of 3 independent experiments. Before performing parametric or non-parametric tests, Normal distribution was assessed. The differences between two groups were evaluated through a parametric two-tailed unpaired Student's T-test, or a non-parametric Mann Whitney test. Instead, for the comparison between more than two groups in Fig. 2B, Kruskal–Wallis followed by Dunn's multiple comparisons test was utilized.

Data availability

The datasets generated during and/or analyzed during the current study are openly available, along with their statistic report, in the Recherche Data Gouv repository, at[61] https://doi.org/10.57745/K4XF9I.

References

1. Sahu, R. et al. Microautophagy of cytosolic proteins by late endosomes. *Dev. Cell* **20**, 131–139 (2011).
2. Wang, L., Klionsky, D. J. & Shen, H. M. The emerging mechanisms and functions of microautophagy. *Nat. Rev. Mol. Cell Biol.* **0123456789**, (2022).
3. Dice, J. F., Chiang, H. L., Spencer, E. P. & Backer, J. M. Regulation of catabolism of microinjected ribonuclease A. Identification of residues 7–11 as the essential pentapeptide. *J. Biol. Chem.* **261**, 6853–6859 (1986).
4. Chiang, H.-L., Terlecky, S. R., Plant, C. P. & Dice, J. F. A Role for a 70-Kilodalton Heat Shock Protein in Lysosomal Degradation of Intracellular Proteins. *Science* **246**, 382–385 (1989).
5. Agarraberes, F. A. & Dice, J. F. A molecular chaperone complex at the lysosomal membrane is required for protein translocation. *J. Cell Sci.* **114**, 2491–2499 (2001).
6. Tekirdag, K. & Cuervo, A. M. Chaperone-mediated autophagy and endosomal microautophagy: Joint by a chaperone. *J. Biol. Chem.* **293**, 5414–5424 (2018).
7. Cuervo, A. M. & Dice, J. F. A receptor for the selective uptake and degradation of proteins by lysosomes. *Science* **273**, 501–503 (1996).
8. Bandyopadhyay, U., Kaushik, S., Varticovski, L. & Cuervo, A. M. The Chaperone-Mediated Autophagy Receptor Organizes in Dynamic Protein Complexes at the Lysosomal Membrane. *Mol. Cell. Biol.* **28**, 5747–5763 (2008).
9. Krause, G. J. et al. Molecular determinants of the crosstalk between endosomal microautophagy and chaperone-mediated autophagy. *Cell Rep.* **42**, 113529 (2023).
10. Vietri, M., Radulovic, M. & Stenmark, H. The many functions of ESCRTs. *Nat. Rev. Mol. Cell Biol.* **21**, 25–42 (2020).
11. Chauhan, A. S. et al. Trafficking of a multifunctional protein by endosomal microautophagy: Linking two independent unconventional secretory pathways. *FASEB J.* **33**, 5626–5640 (2019).
12. Caballero, B. et al. Acetylated tau inhibits chaperone-mediated autophagy and promotes tau pathology propagation in mice. *Nat. Commun.* **12**, 1–18 (2021).
13. Lee, J., Xu, Y. & Ye, Y. Safeguarding lysosomal homeostasis by DNAJC5/CSPα-mediated unconventional protein secretion and endosomal microautophagy. *Front. Cell Dev. Biol.* **10**, 906453 (2022).
14. Kirchner, P. et al. Proteome-wide analysis of chaperone-mediated autophagy targeting motifs. *PLoS Biol.* **17**, 1–27 (2019).
15. Schneider, J. L., Suh, Y. & Cuervo, A. M. Deficient chaperone-mediated autophagy in liver leads to metabolic dysregulation. *Cell Metab.* **20**, 417–432 (2014).
16. Kaushik, S. et al. Chaperone-mediated autophagy regulates adipocyte differentiation. *Sci. Adv.* **8**, eabq2733 (2022).
17. Kaushik, S. & Cuervo, A. M. Degradation of lipid droplet-associated proteins by chaperone-mediated autophagy facilitates lipolysis. *Nat. Cell Biol.* **17**, 759–770 (2015).
18. Bourdenx, M. et al. Chaperone-mediated autophagy prevents collapse of the neuronal metastable proteome. *Cell* **184**, 2696-2714.e25 (2021).
19. Gomez-Sintes, R. et al. Targeting retinoic acid receptor alpha-corepressor interaction activates chaperone-mediated autophagy and protects against retinal degeneration. *Nat. Commun.* **13**, 4220 (2022).
20. Vélez, E. J. et al. Chaperone-mediated autophagy protects against hyperglycemic stress. *Autophagy* **20**, 752–768 (2024).
21. Schnebert, S. *et al.* Chaperone-mediated autophagy in fish: A key function amid a changing environment. https://doi.org/10.1080/27694127.2024.2403956. (2024).
22. Goguet, M. *et al.* The zebrafish as a new model for studying chaperone-mediated autophagy unveils its role in spermatogenesis. *bioRxiv* 2024.06.10.597508 (2024) https://doi.org/10.1101/2024.06.10.597508.
23. Arias, E. & Cuervo, A. M. Pros and cons of chaperone-mediated autophagy in cancer biology. *Trends Endocrinol. Metab.* **31**, 53–66 (2020).
24. Sooparb, S., Price, S. R., Shaoguang, J. & Franch, H. A. Suppression of chaperone-mediated autophagy in the renal cortex during acute diabetes mellitus. *Kidney Int.* **65**, 2135–2144 (2004).
25. Liu, C. et al. Glia maturation factor-β induces ferroptosis by impairing chaperone-mediated autophagic degradation of ACSL4 in early diabetic retinopathy. *Redox Biol.* **52**, 102292 (2022).
26. Kon, M. & Cuervo, A. M. Chaperone-mediated autophagy in health and disease. *FEBS Lett.* **584**, 1399–1404 (2010).
27. Lescat, L. et al. Chaperone-mediated autophagy in the light of evolution: Insight from fish. *Mol. Biol. Evol.* **37**, 2887–2899 (2020).
28. Krause, G. J. et al. Reduced endosomal microautophagy activity in aging associates with enhanced exocyst-mediated protein secretion. *Aging Cell* https://doi.org/10.1111/acel.13713 (2022).
29. Caballero, B. et al. Interplay of pathogenic forms of human tau with different autophagic pathways. *Aging Cell* **17**, 1–17 (2018).
30. Hernández, F. et al. Tau Aggregation. *Neuroscience* **518**, 64–69 (2023).
31. Cuervo, A. M., Knecht, E., Terlecky, S. R. & Dice, J. F. Activation of a selective pathway of lysosomal proteolysis in rat liver by prolonged starvation. *Am. J. Physiol.* **269**, C1200 (1995).
32. Schnebert, S. et al. Diving into the evolutionary history of HSC70-linked selective autophagy pathways: endosomal microautophagy and chaperone-mediated autophagy. *Cells* **11**, 1945 (2022).
33. Uytterhoeven, V. et al. Hsc70-4 deforms membranes to promote synaptic protein turnover by endosomal microautophagy. *Neuron* **88**, 735–748 (2015).
34. Berthelot, C. et al. The rainbow trout genome provides novel insights into evolution after whole-genome duplication in vertebrates. *Nat. Commun.* **5**, 3657 (2014).
35. Pasquier, J. et al. Gene evolution and gene expression after whole genome duplication in fish: The PhyloFish database. *BMC Genomics* **17**, 1–10 (2016).
36. Mesquita, A., Glenn, J. & Jenny, A. (2020) Differential activation of eMI by distinct forms of cellular stress. *Autophagy* https://doi.org/10.1080/15548627.2020.1783833 (2020).
37. Krause, G. J. & Cuervo, A. M. *Assessment of mammalian endosomal microautophagy*. *Methods in Cell Biology* Vol. 164 (Elsevier Inc., 2021).
38. Bolte, S. B. & Cordelieres, F. P. A guided tour into subcellular colocalization analysis in light microscopy. *J. Microsc.* **224**, 213–232 (2006).
39. Chiang, H. L. & Dice, J. F. Peptide sequences that target proteins for enhanced degradation during serum withdrawal. *J. Biol. Chem.* **263**, 6797–6805 (1988).
40. Liu, J. et al. Insights on E1-like enzyme ATG7: Functional regulation and relationships with aging-related diseases. *Commun. Biol.* **2024**(7), 1–15 (2024).
41. Mizushima, N. et al. A protein conjugation system essential for autophagy. *Nature* **395**, 395–398 (1998).
42. Mauthe, M. et al. Chloroquine inhibits autophagic flux by decreasing autophagosome-lysosome fusion. *Autophagy* **14**, 1435–1455 (2018).
43. Mukherjee, A., Patel, B., Koga, H., Cuervo, A. M. & Jenny, A. Selective endosomal microautophagy is starvation-inducible in Drosophila. *Autophagy* **12**, 1984–1999 (2016).
44. Pajares, M. et al. Transcription factor NFE2L2/NRF2 modulates chaperone-mediated autophagy through the regulation of LAMP2A. *Autophagy* **14**, 1310–1322 (2018).
45. Burden, D. A. & Osheroff, N. Mechanism of action of eukaryotic topoisomerase II and drugs targeted to the enzyme. *Biochim. Biophys. Acta* **1400**, 139–154 (1998).

46. Park, C., Suh, Y. & Cuervo, A. M. Regulated degradation of Chk1 by chaperone-mediated autophagy in response to DNA damage. *Nat. Commun.* **6**, 6823 (2015).
47. Kaushik, S. & Cuervo, A. M. Methods to monitor chaperone-mediated autophagy. *Methods Enzymol.* **452**, 297–324 (2009).
48. Kaizuka, T. et al. An autophagic flux probe that releases an internal control. *Mol. Cell* **64**, 835–849 (2016).
49. Morin, G., Pinel, K., Dias, K., Seiliez, I. & Beaumatin, F. RTH-149 cell line, a useful tool to decipher molecular mechanisms related to fish nutrition. *Cells* **9**, 1754 (2020).
50. Shen, C., Yan, J., Jiang, L. S. & Dai, L. Y. Autophagy in rat annulus fibrosus cells: Evidence and possible implications. *Arthritis Res. Ther.* **13**, 1–10 (2011).
51. Mejlvang, J. et al. Starvation induces rapid degradation of selective autophagy receptors by endosomal microautophagy. *J. Cell Biol.* **217**, 3640–3655 (2018).
52. Nguyen, N. T. T., Vincens, P., Dufayard, J. F., Roest Crollius, H. & Louis, A. Genomicus in 2022: Comparative tools for thousands of genomes and reconstructed ancestors. *Nucleic Acids Res.* **50**, D1025–D1031 (2022).
53. Alpern, D. et al. BRB-seq: Ultra-affordable high-throughput transcriptomics enabled by bulk RNA barcoding and sequencing. *Genome Biol.* **20**, 1–15 (2019).
54. Khuong, T. M. et al. Synaptic PI(3,4,5)P3 is required for syntaxin1A clustering and neurotransmitter release. *Neuron* **77**, 1097–1108 (2013).
55. Seiliez, I. et al. Looking at the metabolic consequences of the colchicine-based in vivo autophagic flux assay. *Autophagy* **12**, 343–356 (2016).
56. Piper, R. C. & Katzmann, D. J. Biogenesis and function of multivesicular bodies. *Annu. Rev. Cell Dev. Biol.* **23**, 519–547 (2007).
57. Neikirk, K. et al. Systematic transmission electron microscopy-based identification and 3D reconstruction of cellular degradation machinery. *Adv. Biol.* **7**, 2200221 (2023).
58. Vélez, E. J. et al. Effects of β2-adrenoceptor agonists on gilthead sea bream (*Sparus aurata*) cultured muscle cells. *Comp. Biochem. Physiol. Part A: Mol. Integr. Physiol.* **227**, 179 (2019).
59. Pfaffl, M. W. A new mathematical model for relative quantification in real-time RT-PCR. *Nucleic Acids Res.* **29**, e45 (2001).
60. Seiliez, I. et al. An in vivo and in vitro assessment of autophagy-related gene expression in muscle of rainbow trout (*Oncorhynchus mykiss*). *Comp. Biochem. Physiol. Part B* **157**, 258–266 (2010).
61. Vélez, E. J. & Seiliez, I. DataVenus, V2.0. *Rech. Data Gouv* (2024) https://doi.org/10.57745/K4XF9I.

Acknowledgements

Author contributions

EJV and IS conceived the study, obtained the funding and prepared the first draft. EJV, VV and JG performed the in vitro experiments and laboratory analyses. All authors (EJV, VV, JG, SR, KD, AH, FB, and IS) contributed to the discussion and edition, and approved the final manuscript.

Declarations

Competing interests

The authors declare no competing interests.

Additional information

Supplementary Information The online version contains supplementary material available at https://doi.org/10.1038/s41598-025-23022-x.

Correspondence and requests for materials should be addressed to E.J.V. or I.S.

Reprints and permissions information is available at www.nature.com/reprints.

Publisher's note Springer Nature remains neutral with regard to jurisdictional claims in published maps and institutional affiliations.